Nanoscale Horizons

ROYAL SOCIETY OF CHEMISTRY

COMMUNICATION

View Article Online
View Journal | View Issue

Cite this: *Nanoscale Horiz.*, 2025, 10, 2434

Received 28th April 2025,
Accepted 9th July 2025

DOI: 10.1039/d5nh00280j

rsc.li/nanoscale-horizons

Unraveling interfacial interactions in reduced Nb_2CT_x/GO heterostructures for highly stable and transparent narrow-band photoelectrochemical photodetectors†

Muhammad Abiyyu Kenichi Purbayanto, *[a] Subrata Ghosh, [ab] Dorota Moszczyńska,[c] Carlo S. Casari [b] and Agnieszka Maria Jastrzębska*[a]

The rapid advancement of nanomaterial-based thin-film processing has significantly contributed to the development of multifunctional optoelectronic devices. Among novel nanomaterials, MXenes, 2D transition metal carbides, nitrides, and carbonitrides have garnered substantial attention due to their high optical transparency, tunable optical properties, and excellent electrochemical performance. In particular, niobium carbide (Nb_2CT_x) MXene holds great promise for photoelectrochemical photodetectors (PEC PDs) due to its narrow-band photodetection capability, solution-processing, and stability under light irradiation. However, current Nb_2CT_x-based and 2D-based PEC PDs, in general, suffer from low photocurrent density, limited optical transparency, and poor environmental stability, hindering their practical applications. In this study, we developed a polymeric binder-free transparent reduced Nb_2CT_x/graphene oxide (r-Nb_2CT_x/GO) heterostructured thin film using a facile layer-by-layer technique. Incorporating reduced GO not only assists in improving the electrical conductivity of the heterostructure but also serves as a binder for MXene flakes. We systematically investigate the physicochemical properties of the film, its photodetection, and electrochemical performance. The optimized film exhibits outstanding transparency (70% at 550 nm), narrow-band photodetection response in the ultraviolet region, an excellent photoresponsivity of 50.21 μA W^{-1}, and high environmental stability. Altogether, this study paves the way for developing Nb_2CT_x-based heterostructures for highly sensitive and environmentally stable transparent PEC PDs.

New concepts

Fabricating all-solution-processed thin films based on van der Waals materials holds great potential for constructing large-scale, low-cost, and high-performance optoelectronic devices. However, achieving solution-processed thin films that simultaneously offer high electrical conductivity and excellent transparency remains a significant challenge. By leveraging the outstanding hydrophilicity of both graphene oxide (GO) and Nb_2CT_x MXenes, we develop an innovative approach to fabricate heterostructures *via* a layer-by-layer (LbL) assembly technique. The resulting Nb_2CT_x/GO heterostructures are subsequently reduced using L-ascorbic acid at a low temperature (90 °C). This strategy yields reduced r-Nb_2CT_x/GO (r-Nb_2CT_x/GO) heterostructures exhibiting remarkable oxidation and cycling stability, as well as tunable optical transparency by varying the number of LbL cycles. Simultaneously, the electrical conductivity of the films can be freely adjusted, balancing the trade-off with optical transparency. Using this method, we further developed a transparent photoelectrochemical photodetector operating in the UV region, achieving a transparency of 70% at 550 nm and a high photoresponsivity of 50.21 μA W^{-1}. The superior performance of our novel heterostructure is attributed to several key factors: (i) a moderate and optimized electrical conductivity of the r-Nb_2CT_x/GO films, facilitating efficient electron transport to the current collector, (ii) effective charge separation and transfer across the r-Nb_2CT_x/GO interface, and (iii) enhanced light absorption of r-Nb_2CT_x/GO compared to standalone Nb_2CT_x.

1. Introduction

The breakthrough in graphene discovery in 2004 opened a new application avenue for two-dimensional (2D) atomic crystals.

[a] *Faculty of Mechatronics, Warsaw University of Technology, św. Andrzeja Boboli 8, Warsaw, 02-525, Poland. E-mail: muhammad_abiyyu.kenichi.dokt@pw.edu.pl, agnieszka.jastrzebska@pw.edu.pl*
[b] *Department of Energy, Micro and Nanostructured Materials Laboratory—NanoLab, Politecnico di Milano, via Lambruschini, Milano, 20156, Italy*
[c] *Faculty of Materials Science and Engineering, Warsaw University of Technology, Wołoska 141, Warsaw, 02-507, Poland*

† Electronic supplementary information (ESI) available: Figures: EDS spectra of Nb_2CT_x, GO, and r-Nb_2CT_x/GO. SEM images of Nb_2CT_x/GO. UV-Vis absorption spectra of Nb_2CT_x aqueous dispersion. XRD spectra of Nb_2CT_x, GO, and r-Nb_2CT_x/GO thin films. AFM images of r-Nb_2CT_x/GO thin films. XPS survey and high-resolution spectra of r-Nb_2CT_x/GO. The evolution of electrical resistance of r-Nb_2CT_x/GO thin films by increasing the reduction time. Optical transmittance comparison of Nb_2CT_x, rGO, and r-Nb_2CT_x/GO thin films. The tape adhesion test on r-Nb_2CT_x/GO thin films. The Lorentzian fit of the Raman spectra of fresh and aged Nb_2CT_x and r-Nb_2CT_x/GO thin films. Raman spectra of GO. Current *vs* scan rate curve. The capacity retention of r-Nb_2CT_x/GO thin films. Tables: summary of Nb 3d, C 1s, and O 1s XPS signals for r-Nb_2CT_x/GO thin films. Results from peak fitting for Nb_2CT_x and r-Nb_2CT_x/GO. Photoresponsivity of Nb_2CT_x and r-Nb_2CT_x/GO thin films under different wavelengths. Comparison of the photoresponse performance for PEC photodetectors. See DOI: https://doi.org/10.1039/d5nh00280j

They can be used in advanced optoelectronic devices due to their better mechanical, electronic, and optical properties compared to their bulk counterparts.[1] Moreover, 2D materials offer strong quantum confinement and enhanced interaction with various stimuli, including light, temperature, and spin, making this class of materials intriguing for constructing multifunctional devices with ultra-thin architecture.[2] Over the past decade, extensive efforts have been made to explore novel 2D materials with distinct electronic properties, ranging from metals to insulators, such as transition metal dichalcogenides, hexagonal boron nitride, black phosphorus, perovskite oxides, transition metal carbides and nitrides (MXenes), and transition metal borides (MBenes).[3,4] Among them, MXenes are viewed as potential candidates for building high-performance optoelectronic devices due to their superior electrical conductivity (reaching 2.0×10^4 S cm^{-1}), exceptional light absorption, tunable work function and optoelectronic properties, good mechanical properties, ability to form van der Waals (vdW) heterostructures, and facile solution-processing.[5–7] Recently, Nb_2CT_x MXene has been investigated as a building block in optoelectronic devices due to its exotic fundamental physical properties, such as abnormal strong electron–phonon scattering,[8] ultrafast relaxation charge carrier dynamics,[9] and functional-group tuned superconductivity.[10] For instance, Nb_2CT_x nanosheets show better values of slow and fast relaxation time constants of carrier dynamics (0.5733 ps and 37.4 fs, respectively) compared to $Ti_3C_2T_x$ nanosheets (10.51 ps and 90 fs).[9] Additionally, Nb_2CT_x exhibits a higher extinction coefficient at 808 nm (37.6 L g^{-1} cm^{-1})[11] compared to $Ti_3C_2T_x$ (29.1 L g^{-1} cm^{-1}).[12] Despite this promise, the optoelectronic applications of Nb_2CT_x remain overshadowed by the first discovered MXene, *i.e.*, $Ti_3C_2T_x$, which is relatively easier to synthesize.[13–15]

Recently, 2D-based photoelectrochemical photodetectors (PEC PDs) have become an emerging class of photodetectors due to their simple preparation, cost-effectiveness, and high sensitivity.[16] The photodetection mechanism of PEC PDs is different from that of conventional solid-state PDs. In the case of PEC PDs, both physical (light absorption, photogenerated charge separation, and transport) and chemical processes (redox reactions) play important roles in regulating the photoresponse performance.[16] Additionally, the interaction of electrolyte with the material interface in PEC PDs tunes the unique photoconductivity behaviour that depends on the wavelength of light.[17]

In this sense, Nb_2CT_x has received significant attention as an active material for PEC PDs due to its high specific surface area and narrow-band photoelectric response.[18,19] For example, Gao *et al.* explored the potential of Nb_2CT_x as the PEC PD sensitive to 350–400 nm, with a narrow-band photoresponse. Its photodetection performance could be easily adjusted by controlling the external parameters, such as electrolyte concentrations, bias potential, and light power.[19] However, the performance of these PEC PDs is still far from the merit achieved by their solid-state counterparts, with the responsivity (under 400 nm light) being only 3.74 μA W^{-1} (0.6 V bias voltage and 1 M KOH).

To further improve the photodetection performance of Nb_2CT_x, vdW heterostructures were fabricated to widen the response spectra and prolong the charge carrier lifetime.[13,20] For example, Ren *et al.* developed Nb_2CT_x/SnS_2 PEC PDs with an enhanced photocurrent density of up to 250-fold (3.75 μA cm^{-2}) compared to that of pure Nb_2CT_x (0.015 μA cm^{-2}).[13]

Despite the advancement in Nb_2CT_x-based PEC PDs, several challenges must be tackled to unlock their full potential. For instance, the currently developed Nb_2CT_x and, more broadly, MXene-based PEC PDs lack optical transparency and robust adhesion to the substrate, as the films are simply fabricated using drop-casting methods.[13,19,21,22] Moreover, MXenes suffer from oxidative degradation, which can degrade the device's performance over time, hindering their practical applications.[23] Additionally, polymers were often used as a protective layer as well as binders, which may decrease the electrical conductivity of MXene layers.[24] Recently, layer-by-layer (LbL) assembly of MXene has been developed to fabricate thin films with high adhesion and easily adjusted optoelectronic properties.[25] However, to the best of our knowledge, no study to date has reported the LbL assembly of a transparent thin film for the application as PEC PDs.

In this study, we successfully fabricated polymeric binder-free, transparent, and stable reduced Nb_2CT_x/GO (r-Nb_2CT_x/GO) PEC PDs using LbL assembly *via* a spin-coating technique. We utilized GO nanoflakes as they can facilitate a strong adhesion to the substrate and interfacial and large surface area contacts with MXenes, facilitating a strong adhesion to the substrate.[26] Additionally, using reduced GO in heterostructure formulation gives several benefits, including good barrier properties for mitigating oxidation issues,[27] facilitating efficient photogenerated interfacial charge transfer,[28] and improving electrical conductivity.[26]

Therefore, we performed a detailed investigation of the morphological, structural, electrochemical, and optoelectronic properties of r-Nb_2CT_x/GO to design PEC PDs in a reasonable manner. While compared to pure Nb_2CT_x, we achieved 6.5-fold enhanced photoresponsivity of r-Nb_2CT_x/GO PEC PDs under ultraviolet (UV) irradiation, coupled with narrow-band photodetection features while maintaining optical transparency (70‘% at 550 nm). These findings substantially contribute to the development of Nb_2CT_x-based heterostructures for optoelectronic applications.

2. Results and discussion

In this study, Nb_2CT_x and GO aqueous dispersions were used to fabricate binder-free reduced Nb_2CT_x/GO (r-Nb_2CT_x/GO) thin films for transparent optoelectronic applications. The thin film fabrication process is summarized in Fig. 1. For comparison, Nb_2CT_x thin films were also prepared following the same LbL procedure but without introducing the GO layer. The morphology of bare Nb_2CT_x and GO aqueous dispersion is inspected first. Nb_2CT_x shows a nanoflake structure without large-scale defects, such as holes and superficial oxide particles (Fig. 2a). Moreover, a typical wavy GO flakes continuous over a large area

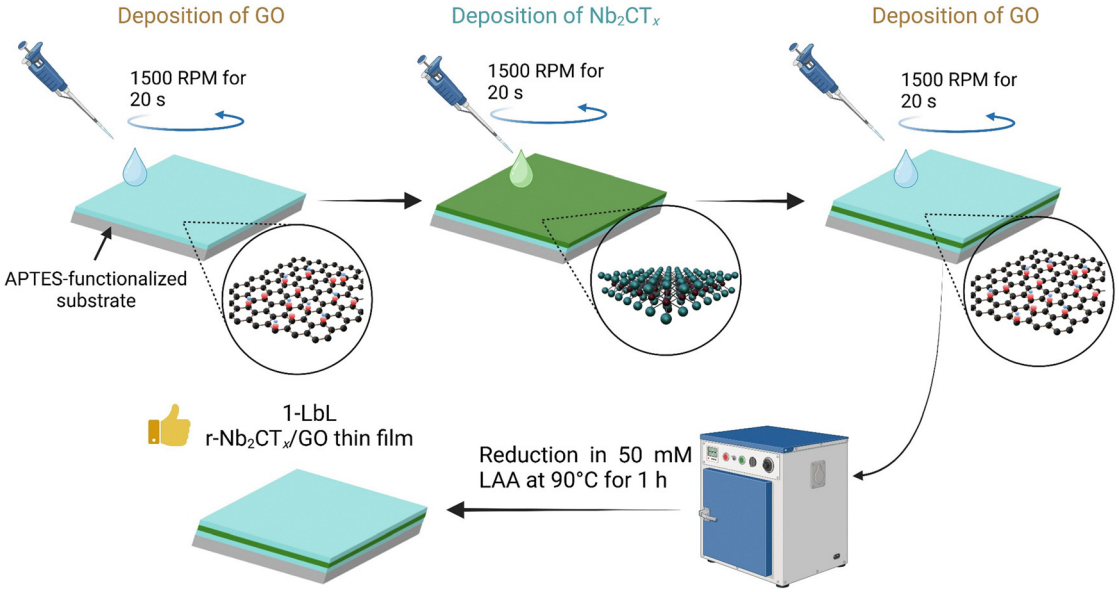

Fig. 1 Schematic of r-Nb_2CT_x/GO thin film fabrication. Partly created with BioRender.com.

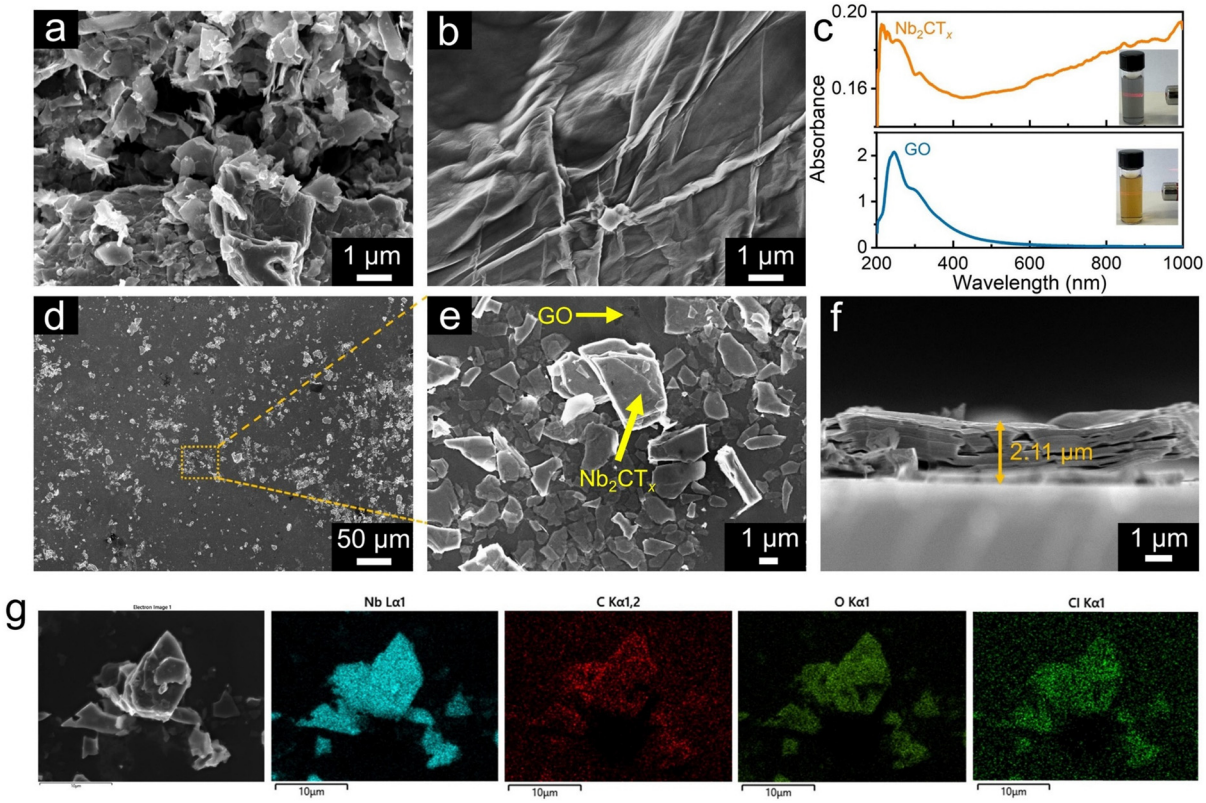

Fig. 2 FESEM images of (a) Nb_2CT_x and (b) graphene oxide (GO). (c) Absorbance spectra of Nb_2CT_x and GO aqueous dispersion at a concentration of 50 μg mL^{-1}. FESEM images of the LbL r-Nb_2CT_x/GO thin film showing (d) surface morphology, (e) the magnified view of the surface, and (f) the cross-sectional view. (g) EDS mapping of r-Nb_2CT_x/GO. The inset of (c) shows the Tyndall effect of Nb_2CT_x and GO aqueous dispersion. 'r' stands for reduced.

with wrinkles is confirmed from Fig. 2b. The EDS spectra of Nb_2CT_x (Fig. S1, ESI†) confirm the presence of Nb, C, O, Cl, and F, with a negligible amount of Al, which might have originated from the residual parental MAX phase. The presence of O, Cl, and F can be connected to the surface functional group on the MXene surface. On the other hand, GO showed the presence of C and O (Fig. S2, ESI†). UV-Vis absorbance measurements of Nb_2CT_x and GO aqueous dispersion are shown in Fig. 2c.

Nb_2CT_x exhibits a broad absorption in the UV and visible regions, and dominant absorption at short wavelengths with an observed band edge at 400 nm, making it suitable for photon absorber use.[19] In contrast, GO is optically transparent in the visible region but exhibits noticeable peaks in the UV region (200–250 nm), which is related to various oxygen functional groups.[29] Both aqueous dispersions showed good colloidal stability, as confirmed by the Tyndall effect (inset of Fig. 2c), making them suitable for fabricating solution-processed thin films without needing surfactants.

X-ray diffraction patterns (XRD) of Nb_2CT_x show the characteristic (002) peak located at 6.8° (Fig. S3a, ESI†), which is in good agreement with previous Nb_2CT_x results.[30,31] In the case of GO, we observe two major peaks located at 10.8° (001) and 27.2° (002) (Fig. S3b, ESI†).[32] These results confirm the high quality of Nb_2CT_x and GO used in this study. Furthermore, the XRD pattern of r-Nb_2CT_x/GO thin films shows the characteristic diffraction peaks of both Nb_2CT_x and GO without the presence of other heterogeneous phases, showing high phase purity and successful formation of the heterostructured thin film (Fig. S4, ESI†). Fig. 2d and e show the surface morphology of LbL r-Nb_2CT_x/GO thin films, which confirms a uniform decoration of Nb_2CT_x flakes on transparent GO layers. The Nb_2CT_x/GO thin film without thermal reduction is shown in Fig. S5 (ESI†). Upon reduction, the Nb_2CT_x is still tightly connected with GO layers, implying a strong interfacial interaction between these materials (Fig. 2d). The cross-sectional images indicated that the r-Nb_2CT_x/GO nanoflakes are well aligned parallelly onto the substrate (Fig. 2f). The EDS elemental mapping (Fig. 2g) of the LbL film shows an even and uniform distribution of Nb, C, O, and Cl elements, which are the constituent elements of the heterostructure. For more details, the EDS spectra of r-Nb_2CT_x/GO thin films and their corresponding quantification are given in Fig. S6 (ESI†). To further confirm the chemical composition and surface chemistry of r-Nb_2CT_x/GO thin films, we carried out X-ray photoelectron spectroscopy (XPS) measurements. The XPS survey spectra (Fig. S7, ESI†) show the strong contribution of C 1s and O 1s compared to Nb 3d, implying that GO is most noticeable at the surface of the film and covers Nb_2CT_x flakes. Notably, C 1s spectra are fitted by five fitting components, as shown in Fig. S8a (ESI†). The peak at 284.5 eV corresponds to sp^2 C–C bonding, while the peaks located at 285.7, 286.6, 287.8, and 288.9 eV can be assigned to sp^3 C–C bonding, C–O, C═O, and COOH, respectively.[33] The high fraction of sp^2 C–C bonding (Table S1, ESI†) shows evidence of GO reduction. At the same time, the low contribution from oxygen-containing functional groups further confirms the partial removal of surface oxygen functionalities of GO.[34] The carbide component, which typically comes from Nb_2CT_x, cannot be clearly identified in C 1s spectra, which might be related to the uniform surface coverage of GO. On the other hand, the Nb 3d signal from Nb_2CT_x can be fitted by a doublet component of Nb^{5+} at 207.5 and 210.3 eV (Fig. S8b, ESI†).[35] The O 1s spectra can be fitted with four components located at 531.1, 532.6, 533.5, and 535.0 eV, corresponding to C–Nb–O_x, C═O, C–O, and adsorbed H_2O at the surface (Fig. S8c, ESI†).[36] The occurrence of C–Nb–O_x implies that Nb_2CT_x in r-Nb_2CT_x/GO is terminated by ═O functional groups. The surface roughness of thin films is critical in optimizing their photodetection performance. AFM topography images (Fig. S9, ESI†) reveal that the r-Nb_2CT_x/GO film exhibits a low root-mean-square roughness of 3.40 nm, indicating a smooth and continuous surface of the fabricated film. A smoother surface can reduce light scattering and ensure more favorable carrier transport and good optical transparency of the film.[4,37]

Raman spectra were measured to further elucidate the crystal structure of MXene. Fig. 3a shows Raman spectra of Nb_2CT and r-Nb_2CT_x/GO thin films. Notably, the MXene region (50–900 cm^{-1}) was fitted to unravel the contribution of each phonon mode (Fig. S9, ESI†). The peaks are assigned based on the experimental computational results of Giordano *et al.* (Table S2, ESI†).[38] The ω_1 (159 cm^{-1}) and ω_3 (258 cm^{-1}) modes can be assigned to in-plane and out-of-plane $Nb_2C(OH)_2$. The ω_2 (209 cm^{-1}) mode corresponds to the phonon mode of out-of-plane Nb_2CO_2. Moreover, the ω_4 (395 cm^{-1}) and ω_5 (507 cm^{-1}) modes correspond to the phonon mode of the –OH functional group, whereas the ω_6 (685 cm^{-1}) mode corresponds to the oxygen functional group. The last peak of ω_7 (745 cm^{-1}) is originated from the phonon mode of C atoms. Altogether, Raman spectra confirm Nb_2CT_x terminated by –OH and ═O groups without the presence of Raman peaks, originating from oxide species. We do not observe the contribution from the phonon modes of the –F terminal group, and the intensity of –OH-related modes is relatively weak. This observation is in line with the previous study, which showed that the ═O group is thermodynamically stable compared to –F and –OH terminal groups on the Nb_2CT_x surface.[39] In the amorphous carbon region (1200–1800 cm^{-1}), we observe broad peaks of D and G bands originating from the disorder-induced peak and in-plane vibration of sp^2 carbon, respectively.[40] The presence of these bands can be related to the synthesis process as reported by other works.[41,42]

In r-Nb_2CT_x/GO thin films, both vibrational modes from Nb_2CT_x and rGO co-exist, confirming the successful fabrication of the heterostructure. We observe the characteristic D-band (1347 cm^{-1}) and G-band (1594 cm^{-1}) of graphitic carbon with strong intensity. Here, the calculated I_D/I_G ratio of r-Nb_2CT_x/GO (1.24) is higher than those of GO (0.78) and Nb_2CT_x (0.72) (Fig. S10, ESI†), indicating the formation of defects during the reduction process and the decrease of oxidation levels in GO.[43] Lower full width at half maximum of the D-band and G-band of r-Nb_2CT_x/GO than that of Nb_2CT_x is also observed (Table S3, ESI†), indicating that the dominant features of sp^2-carbon come from rGO and also the reduction process induced graphitization of amorphous carbon. Additionally, the characteristic phonon modes of Nb_2CT_x are preserved without noticeable niobium oxide-related vibrations. Fig. S11 (ESI†) shows the curve fitting of Raman modes for r-Nb_2CT_x/GO in the MXene region. Most of the peaks in the low-frequency region are blue-shifted compared to Nb_2CT_x (Table S4, ESI†), which might be caused by interfacial charge redistribution and structural modification of Nb_2CT_x upon hybridization with rGO.[38,44,45]

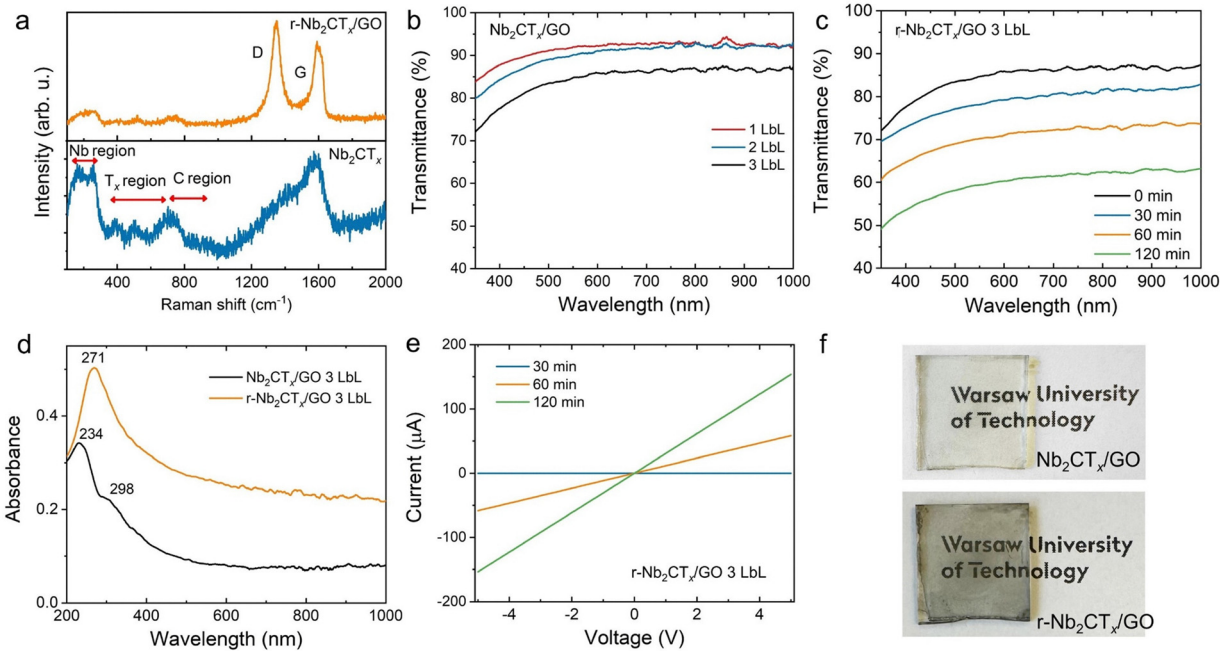

Fig. 3 (a) Raman spectra of Nb_2CT_x and r-Nb_2CT_x/GO. Transmittance of (b) Nb_2CT_x/GO with different LbL numbers and (c) different reduction times. (d) Absorbance spectra of Nb_2CT_x and r-Nb_2CT_x/GO. (e) *I–V* curve of r-Nb_2CT_x/GO with varying reduction time. (f) Digital photographs of Nb_2CT_x/GO and r-Nb_2CT_x/GO, showing the successful reduction.

We observe an interesting observation in the surface termination region, where ω_6 intensity is markedly increased in comparison to ω_7, indicating that the =O functional group becomes more dominant in the heterostructure compared to the Nb_2CT_x counterpart.

To employ the materials for optoelectronic applications, a material should have excellent optical and electrical properties. We monitored the optical transmittance changes on Nb_2CT_x/GO, acting as a starting film before reduction (Fig. 3b). The optical transmittance of Nb_2CT_x/GO decreases across the entire measured wavelength range as the number of coating layers increases, indicating that the film absorbs both UV and visible light more. Fig. 3c shows the effect of reduction time on the optical transmittance of Nb_2CT_x/GO-3, where transparency is decreased by increasing the reduction time. The absorption spectra of Nb_2CT_x/GO-3 showed two distinct peaks located at 234 and 298 nm (Fig. 3d), which are the fingerprints of GO. The former is originated from π–π* transitions of C=C in amorphous carbon, while the latter is connected to n–π* transitions in C=O bonds.[46] After reduction, only a single peak located at 271 nm is observed.[47] This fact ensures a successful transformation from Nb_2CT_x/GO to r-Nb_2CT_x/GO.

To assess the evolution of electrical conductivity upon reduction, we performed *I–V* measurements of $Nb_2C_2T_x$ by varying reduction time (Fig. 3e). In particular, the Nb_2CT_x/GO-3 showed no observable *I–V* curve owing to low electrical conductivity exceeding the measurement limit of the source meter, hence not shown in the figure. We begin to observe the Ohmic *I–V* response by performing 30 minutes of reduction, and the electrical conductivity keeps increasing by prolonging the reduction time. The calculated resistance of r-Nb_2CT_x/GO-3 obtained by 30 minutes reduction is 1.72 GΩ, and it markedly decreased to 85.62 kΩ for 60 minutes of reduction and 32.52 kΩ for 120 minutes of reduction (Fig. S12, ESI†). At the same time, we observe a trade-off between optical transparency and electrical conductivity. It should be noted that at least ~70% transparency should be maintained to use a material for transparent optical applications.[48] Since the transmittance of r-Nb_2CT_x/GO-3 (70% at 550 nm) falls between that of Nb_2CT_x (75%) and rGO (61%) (Fig. S13, ESI†), and it shows good electrical conductivity, we choose r-Nb_2CT_x/GO-3 with 30 minutes of reduction for further analysis. The good optical transparency of the r-Nb_2CT_x/GO film is also evidenced by digital photography, where the film maintains its transparency after reduction (Fig. 3f). Interestingly, the reduction procedure does not cause peeling of the Nb_2CT_x/GO thin film, as confirmed from the tape adhesion test (Fig. S14, ESI†). The film shows minimal peeling after testing, even in the absence of a polymeric binder in the fabrication process. This fact cannot be achieved with regular drop-casting or spray-coating methods, where polymeric binders are used.[49,50]

We then tested the environmental stability by assessing the electrical conductivity of the thin film over time and monitoring the change of Raman spectra after storing the sample under ambient conditions.[51,52] This method is more accurate and straightforward than the common method, which measures the change of the optical absorbance of the film.[25] Fig. 4a shows that Nb_2CT_x loses electrical conductivity over time, as indicated by an increase in the resistivity (R/R_0). Whereas, r-Nb_2CT_x/GO shows a negligible change in resistivity, indicating a high

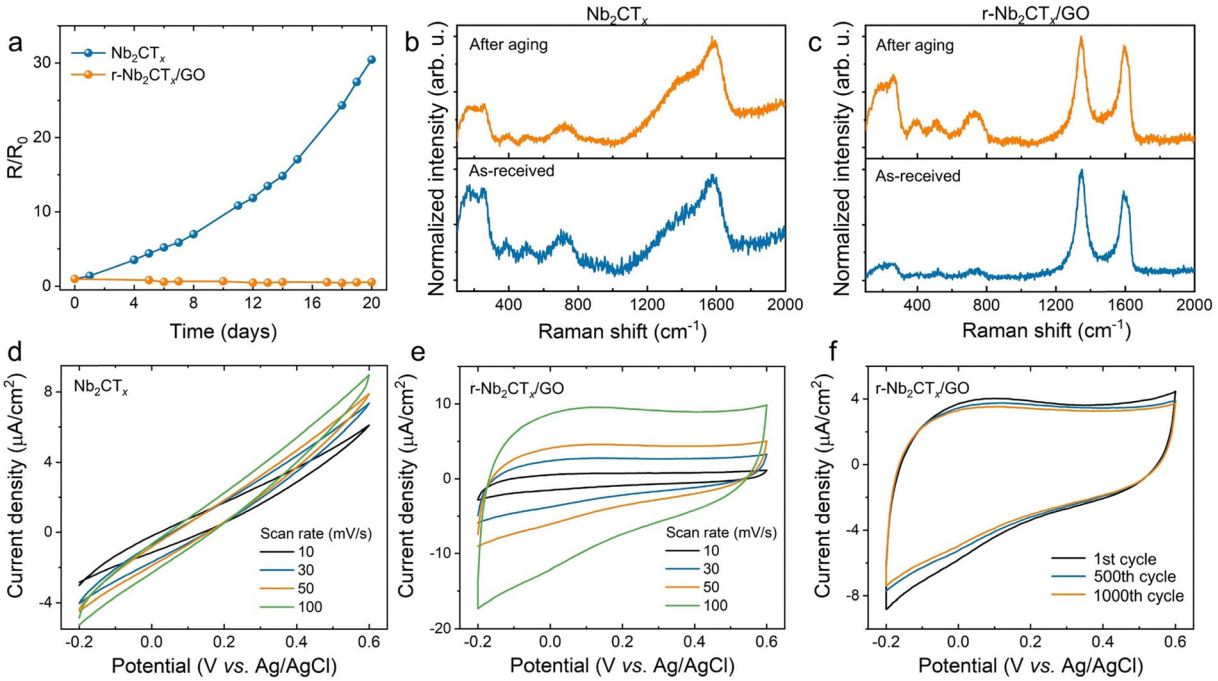

Fig. 4 (a) Evolution of the relative resistance of Nb_2CT_x and r-Nb_2CT_x/GO measured over time. Raman spectra of (b) Nb_2CT_x and (c) r-Nb_2CT_x/GO after aging. The CV curve of (d) Nb_2CT_x and (e) r-Nb_2CT_x/GO at different scan rates. (f) Cycling stability of r-Nb_2CT_x/GO at a scan rate of 50 mV s^{-1} up to 1000 CV cycles.

oxidation stability of this heterostructure. This high stability is attributed to the greater hydrophobicity of rGO compared to MXenes, along with its low gas and water permeability in ambient air.[26,27] Additionally, the stabilization effect could be attributed to the removal of O^{2-} ions in the carbon sites of MXenes using L-ascorbic acids, resulting in lower nucleation sites for metal oxides' growth.[53]

From the Raman measurement after aging under ambient conditions, the most striking feature observed in aged-Nb_2CT_x is the significant amplification of D- and G-bands relative to the peaks in the low-frequency region, indicating the dominance of amorphous carbon (Fig. 4b). An increased graphitization is observed in aged-Nb_2CT_x, where we observe a blue shifting of D- and G-bands and an increment in I_D/I_G (Table S5, ESI†).[54] Fitting analysis in the low-frequency region (Fig. S15, ESI†) reveals a blueshift in the ω_1, ω_2, ω_3, ω_5, and ω_6 peaks, suggesting partial oxidation of Nb atoms. In contrast, ω_7 exhibits a redshift. These peaks slightly shift by 1–6 cm^{-1}, indicating surface modification upon aging. Furthermore, the ω_1/ω_3 ratio is an important parameter to quantify the changes in Nb_2CT_x surface chemistry of Nb_2CT_x due to degradation. In aged-Nb_2CT_x, ω_1 becomes dominant, resulting in increased ω_1/ω_3 from 0.89 to 1.04, providing evidence for carbon network disruption (Table S6, ESI†).[38]

On the other hand, in the case of r-Nb_2CT_x/GO, we cannot assess the evolution of amorphous carbon originating from MXene upon aging, as it is overshadowed by a strong signal from rGO. However, the degradation study of heterostructures can still be monitored through fitting analysis in the low-frequency region (Fig. S16, ESI†). From the fitting results, we observe a large redshift of all peaks, ranging from 3 to 22 cm^{-1}, which can be attributed to the removal of intercalated water or changes in surface functionalities (Table S4, ESI†).[38,55] On the other hand, the relative intensity of ω_1 remains largely unchanged, in contrast to aged-Nb_2CT_x, indicating minimal sample degradation (Table S6, ESI†). Thus, the Raman analysis supports the finding of electrical measurement results, in which the oxidation stability of Nb_2CT_x is improved by creating an interfacial contact with rGO.

After successfully fabricating an optically transparent and environmentally stable r-Nb_2CT_x/GO, we explore its multifunctionality as an active electrode in PEC PDs. The previous study shows that Nb_2CT_x exhibits a strong absorption from UV to near-infrared regions, making it promising as a building block for various optoelectronic devices.[19] First, we performed cyclic voltammetry (CV) measurements to analyze the electrochemical properties of the thin film. The CV response of Nb_2CT_x shows no observable redox peak, with the current densities increasing with an increase in the scan rate (Fig. 4d). Bare Nb_2CT_x is resistive in nature as the CV response is not parallel with the voltage-axis and more inclined towards the current-axis, which is in agreement with the electrical properties. Moreover, r-Nb_2CT_x/GO shows a more rectangular CV response, implying better ionic and electronic transport within the film structure than Nb_2CT_x alone (Fig. 4e). Additionally, the CV curve retains its quasi-rectangular shape upon scan rate increment. We further calculate the areal capacitance (C_A) from the CV curve by taking the linear fitting of current density under various scan rates, as shown in Fig. S17 (ESI†). Notably, r-Nb_2CT_x/GO showed significant improvement in the C_A value (84.21 μF cm^{-2}) compared

to Nb_2CT_x (32.90 μF cm^{-2}). The C_A of r-Nb_2CT_x/GO is larger than other transparent films, such as $Ti_3C_2T_x$ (75.2 μF cm^{-2} with 80% optical transparency),[56] and graphene (12.4 μF cm^{-2} with 67% optical transparency).[57] A relatively high C_A in r-Nb_2CT_x/GO opens the possibility of being used as a transparent energy-storage device. Furthermore, we examined the stability of r-Nb_2CT_x/GO by performing continuous CV cycling (Fig. 4f). Here, the film shows good stability, with a capacity retention of 89% after 1000 cycles (Fig. S18, ESI†).

To study the electron transport of the heterostructure, the electrochemical impedance spectroscopy (EIS) spectra have been measured. Fig. 5a shows the Nyquist plot of Nb_2CT_x and r-Nb_2CT_x/GO. In the case of Nb_2CT_x, a large semicircle is observed, indicating charge transfer between the film surface and the electrolyte. The r-Nb_2CT_x/GO curve depicts the absence of a semicircle in the high-frequency region. However, we observe that the imaginary part of the impedance spectra changes rapidly moving away from the real axis, indicating an excellent electrical conductivity of the film.[58] r-Nb_2CT_x/GO (13.18 Ω) exhibits a lower equivalent series resistance compared to Nb_2CT_x (17.85 Ω). This positive effect can significantly enhance the photoresponse and stability of r-Nb_2CT_x/GO as photoelectrochemical PEC PDs. The properties of the films were tested in a three-electrode measurement setup using 0.5 M Na_2SO_4 as an electrolyte, as illustrated in Fig. 5b. To investigate the performance of PEC PDs, we measured the photocurrent density of Nb_2CT_x and r-Nb_2CT_x/GO under UV light irradiation (Fig. 5c). In particular, the r-Nb_2CT_x/GO heterostructure exhibited a 2.8-fold higher photocurrent (0.65 μA cm^{-2}) with a typical stable on–off cycling under UV irradiation compared to Nb_2CT_x (0.23 μA cm^{-2}). The high photodetection performance of r-Nb_2CT_x/GO is attributed to the improved electrical conductivity and light absorption of the film. Thus, heterostructure formation provides efficient light harvesting, accelerated transport of photogenerated charge carriers, and enhanced charge separation efficiency.[59,60] Next, to further quantify the photodetection performance of the films, we calculate their photoresponsivity under different light wavelengths (Fig. 5d).

The obtained photoresponsivity values for Nb_2CT and r-Nb_2CT_x/GO are summarized in Table S7 (ESI†). Both films exhibited a dominant photoresponsivity under UV light (365 nm). A lower photoresponsivity is also observed under violet (395 nm) and blue light (457 nm), where the photoresponse is considerably low beyond this wavelength. Therefore, these results indicate that Nb_2CT_x and r-Nb_2CT_x/GO effectively harvest photons in the short wavelength (365 nm), whereas no noticeable photoresponse is observed for wavelengths longer than 457 nm. A similar narrow band (350–400 nm) photoresponse behavior of Nb_2CT_x was also reported previously.[19]

Additionally, Gao *et al.* calculated the work function of –OH-terminated Nb_2CT_x to be 3.33 eV, corresponding to the critical wavelength of dominant photoresponsivity, *i.e.*, 365 nm.[19] The calculated photoresponsivity of Nb_2CT_x is 7.75 μA W^{-1} at 365 nm, which is significantly enhanced in r-Nb_2CT_x/GO, reaching 50.21 μA W^{-1} (a 6.5-fold enhancement). Note that

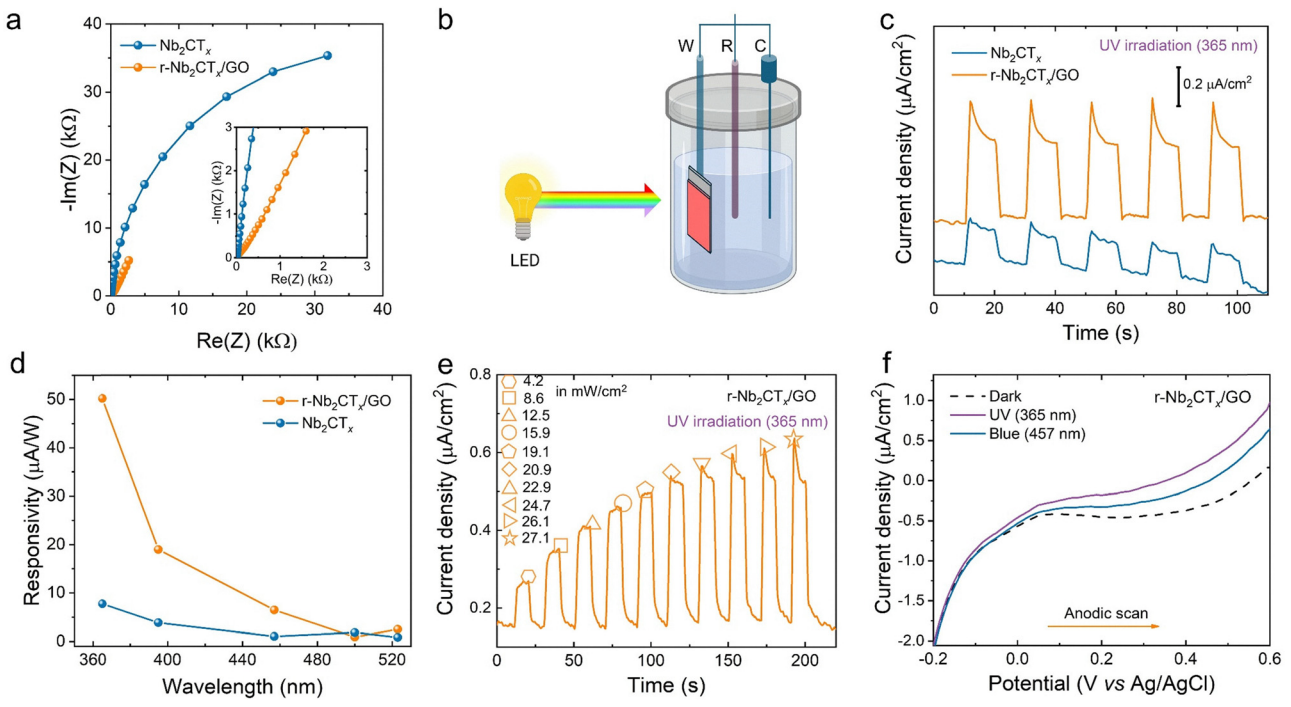

Fig. 5 (a) Nyquist plot of Nb_2CT_x and r-Nb_2CT_x/GO. (b) Schematic illustration of photoelectrochemical measurements of the thin films. (c) Photoresponse comparison of Nb_2CT_x and r-Nb_2CT_x/GO under UV irradiation at a bias potential of 0.6 V. (d) Photoresponsivity of Nb_2CT_x and r-Nb_2CT_x/GO towards different LED wavelengths. (e) Photoresponse behavior of r-Nb_2CT_x/GO under UV irradiation with various light power densities at a bias potential of 0.6 V. (f) LSV curves of r-Nb_2CT_x/GO under UV and blue light irradiation.

the photoresponsivity value of r-Nb_2CT_x/GO is much higher than previously reported Nb_2CT_x PEC PDs, which exhibited 12.6 μA W^{-1} at 1 M KOH.[19]

In order to further explore the performance of the r-Nb_2CT_x/GO PEC PDs, we measured the photoresponse under UV light irradiation with different light powers, as depicted in Fig. 5e. Here, the photocurrent density of r-Nb_2CT_x/GO can be increased almost linearly as we increase the illuminated light power, owing to more photogenerated electron and hole pairs.[61] In particular, a 2.3-fold photocurrent enhancement can be achieved by increasing the light power from 4.2 to 27.2 mW cm^{-2}. Interestingly, as the light power increases, we start to observe a sharp transient peak at a light power of 20.9 mW cm^{-2}, which further signifies the highest laser power (27.1 mW cm^{-2}). The peak further exponentially drops and stabilizes over time before it falls to a dark current when the light is chopped off. This sharp and instantaneous transient peak is attributed to the capacitive current, in which the PDs are rapidly charged when illuminated by relatively large light power. This behavior can be connected to charge accumulation phenomena at the heterostructure interface.[62] Therefore, the photoresponse of r-Nb_2CT_x/GO can be tuned by varying light power.

To further evaluate the PEC PD performance, we measured linear sweep voltammograms (LSV) at a scan rate of 10 mV s^{-1}. Fig. 5f shows the LSV curves of r-Nb_2CT_x/GO in the dark and under UV or blue light irradiation. The results indicate that no noticeable redox peaks are observed across the measured potential range. We also observe the presence of anodic photocurrent, with a more pronounced increase in current density under irradiation with UV compared to blue light. Table S8 (ESI†) compares the photoresponse performance of r-Nb_2CT_x/GO with other state-of-the-art nanomaterial-based PEC PDs. Notably, r-Nb_2CT_x/GO demonstrates high photoresponsivity while maintaining excellent optical transparency, which is not commonly achieved in conventional PEC PDs, as most developed PEC PDs are opaque in visible light. This combination makes r-Nb_2CT_x/GO suitable for see-through optoelectronic devices. Although some studies have attempted to develop transparent PEC PDs, they often suffer from limited visible light transmittance (<60%), complex fabrication procedures, and sluggish photoresponsivity.[63–65] Herein, the high photodetection performance of r-Nb_2CT_x/GO can be attributed to several key factors, including (i) a moderate and optimized electrical conductivity of r-Nb_2CT_x/GO, facilitating faster electron transport to the current collector, (ii) efficient charge separation and transfer across the r-Nb_2CT_x/GO interface, and (iii) enhanced light absorption of r-Nb_2CT_x/GO compared to standalone Nb_2CT_x, as observed in the UV-Vis results.[26,45] Altogether, this study demonstrates the promise of r-Nb_2CT_x/GO thin films for transparent and highly stable PEC PDs in which the photoresponse performance can be easily tuned by changing the external parameters.

3. Conclusions

In conclusion, we have successfully fabricated transparent reduced-Nb_2CT_x/graphene oxide (r-Nb_2CT_x/GO) heterostructured thin films *via* a layer-by-layer (LbL) technique and studied their fundamental optoelectronic properties for use as photoelectrochemical photodetectors (PEC PDs). The r-Nb_2CT_x/GO thin films exhibited excellent optical transparency (70% at 550 nm) coupled with electrical conductive properties, in which these properties can be easily tuned by varying LbL numbers. The developed films possessed a good uniformity that cannot be achieved in conventional MXene films obtained by drop-casting or spray-coating methods. We also observed parameter enhancement while hybridizing Nb_2CT_x with rGO, including high environmental stability, as revealed by minimal changes in the crystal structure, and stable electrical performance when the thin films were stored under ambient conditions. This high stability can be connected to the great hydrophobicity of rGO, along with its low gas and water permeability.

In the case of the photoelectrochemical response, the developed r-Nb_2CT_x/GO PEC PDs show a highly stable cycling performance, as indicated by 89% capacity retention after 1000 cycles. Additionally, the r-Nb_2CT_x/GO PEC PDs showed narrow-band photosensitivity in the UV region, with responsivity enhanced 6.5-fold compared to that of solo Nb_2CT_x, which further underscores the importance of adding rGO in facilitating more efficient light harvesting and photogenerated charge separation and transport. Interestingly, the photoresponse behavior of the PDs can be easily tuned by changing the light power, where we start to observe capacitive current at high incident light power. Altogether, our results open a new insight into the exploration of transparent and binder-free MXene-based PEC PDs, paving the way toward their use in advanced optoelectronic devices. The transparency of PEC PDs can be further enhanced without compromising electrical conductivity by controlling MXene surface chemistry and fabricating thin films composed of large-sized (micron-scale) MXene flakes, which help in reducing interflake resistance.

4. Experimental

4.1. Materials

Delaminated Nb_2CT_x MXene paste was acquired from Carbon-Ukraine. L-Ascorbic acid (LAA, 99% purity), phosphoric acid (H_3PO_4, 85 wt%), sulfuric acid (H_2SO_4, 98 wt%), potassium permanganate ($KMnO_4$), and Hellmanex III were purchased from Sigma-Aldrich. 3-Aminopropyltriethoxysilane (APTES, 99%) was purchased from Thermo Scientific Chemicals. Anhydrous sodium sulfate (Na_2SO_4) was purchased from Chempur. Ethanol (99.8% purity) was purchased from POCH. Isopropanol (99.9% purity) and glass substrates were purchased from Chemland. Indium tin oxide (ITO)-coated glass substrates were purchased from 3D Nano, Poland. P-type silicon wafers (100) were purchased from Microshop, Poland. Double distilled water (DDW) was used in this study.

4.2. Synthesis of graphene oxide

Graphene oxide (GO) was synthesized by modified Hummers' method. In detail, 5 g of graphite flakes were mechanically stirred (180 rpm for 1 h) in the mixed solution of 110 mL of 98 wt% H_2SO_4 and 11.5 mL of 85 wt% H_3PO_4. Thereafter, 15 g

of $KMnO_4$ was gradually added to the reaction mixture in an ice/water bath (5 °C) and then stirred for 24 h at room temperature. Finally, the product was washed repeatedly with DDW by centrifugation until the pH reached ~6.

4.3. Thin film preparation

First, the 15 mm × 15 mm substrates (glass, quartz, or ITO) were sonicated in 2 vol% Hellmanex solution for 20 minutes at 40 °C. Next, the substrates were rinsed with isopropanol, followed by DDW. The substrates were then dried in a hotplate at 80 °C for 5 minutes. To promote substrate hydrophilicity, the substrate was treated with UV-O_3 for 1 hour. The substrates were immersed in 2 vol% APTES in absolute ethanol for 30 minutes at room temperature to enhance the interaction between the substrate and the material.[66] The loosely bonded APTES was thoroughly removed by rinsing the substrates with ethanol and DDW. 2 mg mL^{-1} aqueous dispersion of Nb_2CT_x and GO was used as the coating ink. The coating ink was prepared by uniformly dispersing it in a bath sonicator for 5 minutes (EMAG Emmi 20 HC, 150 W). The thin films were then fabricated *via* the spin coating technique (Ossila spin coater), where 60 μL of the ink was dispensed per cycle (1500 rpm, 20 seconds). The thin films were fabricated using a layer-by-layer (LbL) assembly technique, where 1 LbL is composed of the GO/Nb_2CT_x/GO sandwich structure, following the same structure proposed by Karmakar *et al.*[51] The fabricated thin film is labeled as Nb_2CT_x/GO-*n*, where *n* is the number of LBL. The obtained Nb_2CT_x/GO thin films were then reduced using a facile thermal annealing-assisted LAA treatment. Briefly, as-prepared films were immersed in 50 mM of LAA solution and heated at 90 °C for 1 hour. Finally, the reduced Nb_2CT_x/GO (r-Nb_2CT_x/GO) films were thoroughly rinsed with DDW to remove residual LAA and loosely bonded Nb_2CT_x or GO nanoflakes.

4.4. Physical characterization

The morphology of thin films was investigated using field emission scanning electron microscopy (FESEM, ZEISS SUPRA 40, Jena, Germany). For the FESEM characterization, the thin films were deposited on Si substrates. The film's elemental analysis was analyzed using energy-dispersive X-ray spectroscopy (EDS). X-ray diffraction (XRD) patterns were acquired using a Bruker D8 advanced diffractometer using Cu Kα radiation 0.154 nm (Bruker, Billerica, MA). The measurements were recorded in 2θ mode, while the incidence angle was fixed at 0.2° (grazing-incidence mode), with a step size of 0.025° and a scan time of 5 s. The surface topography of thin films was studied using a NX10 (Park Systems, Korea) atomic force microscope (AFM). Measurements were taken in the non-contact mode at room temperature. Scanning was performed over 5 μm × 5 μm area with a resolution of 512 pixels, and the scanning speed was set to 0.3 Hz. An all-In-One D (Budgetsensors, Bulgaria) cantilever with a force constant of 40 N m^{-1} was used during measurements. All images and data were processed and calculated using Gwyddion software.

X-ray photoelectron spectroscopy (XPS) measurements were conducted using a PHI 5000 VersaProbe II Scanning ESCA Microprobe (ULVAC-PHI; Japan) spectrometer. The XPS spectra were obtained under the following conditions: monochromatic Al-Kα radiation ($h\nu$ = 1486.6 eV), an X-ray source operating at 25 W, 15 kV, and a 100 μm spot size, and an area of 500 μm^2. High-resolution XPS spectra were collected with an energy step size of 0.1 eV and an analyzer pass energy of 23.5 eV. The obtained XPS spectra were analyzed using CasaXPS software (v.2.3.22, Casa Software Ltd, United Kingdom) using the sensitivity factors native for the hardware. Deconvolution of all high-resolution XPS spectra was performed using a Shirley background and a Gaussian peak shape with 30% Lorentzian character. The Raman spectra of the films were recorded using a Renishaw InVia Raman spectrometer with a 514.5 nm laser and 1800 lines per mm grating spectrometer. We used a 50× microscope objective, 10 seconds of acquisition time, 10 accumulations, and a low laser power of 0.4 mW to avoid laser-induced damage to the samples. The spike caused by cosmic rays was removed using the single-spectrum spike removal algorithm developed by Coca-Lopez *et al.*[67] For Raman peak analysis, the recorded Raman spectra were baseline-subtracted and fitted using a Lorentzian function.[68] Multiple spectra were recorded at different spots on the same sample, and the error was calculated as the standard deviation.

4.5. Optoelectronic property measurements

The optical properties of the thin films were measured using a double-beam UV-Visible (UV-Vis) spectrometer (Evolution 220, Thermo Scientific), where a blank glass was used as the reference for spectral measurements. The UV-Vis spectra were recorded with an integration time of 0.1 seconds, a scanning speed of 600 nm per minute, and a wavelength resolution of 1 nm. Herein, the light was incident on the film side of the substrates. Moreover, we also deposited the thin film on a quartz substrate to study the reduction of Nb_2CT_x/GO in detail. For electrical measurements, the thin films were deposited on glass substrates, and silver paste was applied to the edges with a 1 cm spacing to enable two-probe measurements. The corresponding current–voltage (*I*–*V*) curves were measured using a source meter unit (Keithley SMU 2450, USA), over a voltage range of −5 to 5 V. To assess the environmental stability, the thin films were stored under ambient conditions, and their electrical resistance was monitored over time using a digital multimeter (Keithley DAQ 6510, USA). Additionally, the Raman spectra of Nb_2CT_x and r-Nb_2CT_x/GO were recorded after 15 and 17 days of ambient exposure to monitor sample degradation through monitoring the structural and surface chemistry changes in the materials.[55]

4.6. Electrochemical measurements

The electrochemical properties of the films were measured in three-electrode systems using a Metrohm Dropsens potentiostat (μStat-i 400s, Asturias, Spain). The binder-free r-Nb_2CT_x/GO films coated on the ITO substrate served as the working electrode, while an Ag/AgCl (in 3 M KCl) and a platinum wire were employed as the reference and counter electrodes,

respectively. Electrochemical measurements were conducted using 0.5 M Na_2SO_4 as the electrolyte.

Cyclic-voltammetry (CV) was measured within a voltage window of −0.2 to 0.6 V *vs.* Ag/AgCl with different scan rates ranging from 10 to 100 mV s^{-1}. Before measurements, a conditioning step of 10 cyclic CV was performed with a scan rate of 50 mV s^{-1}. This conditioning was intended to promote the penetration of electrolytes into electrodes.[69] The areal capacitance (C_A) is estimated by performing the linear fitting of current density *vs.* scan rate, according to eqn (1):

$$C_A = \frac{(dQ/dt)}{(dE/dt)} = \frac{i}{SR} \quad (1)$$

where C_A, i, and SR are the areal capacitance, current, and scan rate, respectively. The electrochemical impedance spectroscopy (EIS) measurement was performed at the open circuit voltage under the dark conditions within the frequency range of 0.1–100 kHz and an alternative current amplitude of 10 mV.

The photoelectrochemical (PEC) study was conducted by irradiating the thin films with an LED source (Photocube, Photochemical reactor, ThalesNano, Budapest), at various wavelengths, including 365, 395, 457, 500, 523, and 625 nm. The light intensity was calibrated with an optical power meter equipped with a Si sensor (Thorlabs, PM120VA). Chronoamperometry measurements were recorded at 0.6 V *vs.* Ag/AgCl with an interval of 0.5 seconds. Furthermore, linear sweep voltammetry (LSV) was scanned in an anodic direction with a scan rate of 10 mV s^{-1} under dark conditions and irradiation.

Author contributions

MAKP designed the experiments, prepared and characterized the samples, collected and analyzed the results, prepared figures, and writing the original manuscript draft; SG performed SEM and Raman measurements; DM performed XRD measurements; CSC corrected the original manuscripts; AMJ supervised the preparation of the manuscript and corrected the original manuscript. All the authors contributed to the writing of the manuscript.

Conflicts of interest

There are no conflicts of interest to declare.

Data availability

The data supporting this study are available in the Repository for Open Data at **https://doi.org/10.18150/B64K08**.

Acknowledgements

This work was funded by the National Science Centre (NCN) within the framework of the research projects 'PRELUDIUM-21' (UMO-2022/45/N/ST5/02472) and 'OPUS 23' (2022/45/B/ST5/03652). Fig. 1 and graphical abstract are partly created with BioRender.com.

References

1 K. F. Mak and J. Shan, Photonics and Optoelectronics of 2D Semiconductor Transition Metal Dichalcogenides, *Nat. Photonics*, 2016, **10**(4), 216–226, DOI: **10.1038/nphoton.2015.282**.

2 Q. Liu, S. Cui, R. Bian, E. Pan, G. Cao, W. Li and F. Liu, The Integration of Two-Dimensional Materials and Ferroelectrics for Device Applications, *ACS Nano*, 2024, **18**(3), 1778–1819, DOI: **10.1021/acsnano.3c05711**.

3 M. A. K. Purbayanto, M. Chandel, M. Birowska, A. Rosenkranz and A. M. Jastrzębska, Optically Active MXenes in van der Waals Heterostructures, *Adv. Mater.*, 2023, 2301850, DOI: **10.1002/adma.202301850**.

4 M. Deng, Z. Li, S. Liu, X. Fang and L. Wu, Wafer-Scale Integration of Two-Dimensional Perovskite Oxides towards Motion Recognition, *Nat. Commun.*, 2024, **15**(1), 8789, DOI: **10.1038/s41467-024-52840-2**.

5 R. Yu, H. Qiao, G. Liao, Z. Huang, Q. Bao and X. Qi, Chloroplast-Inspired Carrier Circulation for Improved Photoelectrochemical Photodetectors Based on Ti_2CT_x Nanosheets, *ACS Appl. Mater. Interfaces*, 2023, **15**(42), 49545–49553, DOI: **10.1021/acsami.3c12800**.

6 M. A. K. Purbayanto, V. Presser, K. Skarżyński, M. Słoma, M. Naguib and A. M. Jastrzębska, MXenes: Multifunctional Materials for the Smart Cities of Tomorrow, *Adv. Funct. Mater.*, 2024, 2409953, DOI: **10.1002/adfm.202409953**.

7 J. Chen, X. Liu, Z. Li, F. Cao, X. Lu and X. Fang, Work-Function-Tunable MXenes Electrodes to Optimize p-$CsCu_2I_3$/*n*-$Ca_2Nb_{3-x}Ta_xO_{10}$ Junction Photodetectors for Image Sensing and Logic Electronics, *Adv. Funct. Mater.*, 2022, **32**(24), 2201066, DOI: **10.1002/adfm.202201066**.

8 Y. Huang, J. Zhou, G. Wang and Z. Sun, Abnormally Strong Electron–Phonon Scattering Induced Unprecedented Reduction in Lattice Thermal Conductivity of Two-Dimensional Nb_2C, *J. Am. Chem. Soc.*, 2019, **141**(21), 8503–8508, DOI: **10.1021/jacs.9b01742**.

9 L. Gao, H. Chen, F. Zhang, S. Mei, Y. Zhang, W. Bao, C. Ma, P. Yin, J. Guo, X. Jiang, S. Xu, W. Huang, X. Feng, F. Xu, S. Wei and H. Zhang, Ultrafast Relaxation Dynamics and Nonlinear Response of Few-Layer Niobium Carbide MXene, *Small Methods*, 2020, **4**(8), 2000250, DOI: **10.1002/smtd.202000250**.

10 V. Kamysbayev, A. S. Filatov, H. Hu, X. Rui, F. Lagunas, D. Wang, R. F. Klie and D. V. Talapin, Covalent Surface Modifications and Superconductivity of Two-Dimensional Metal Carbide MXenes, *Science*, 2020, **369**(6506), 979–983, DOI: **10.1126/science.aba8311**.

11 H. Lin, S. Gao, C. Dai, Y. Chen and J. Shi, A Two-Dimensional Biodegradable Niobium Carbide (MXene) for Photothermal Tumor Eradication in NIR-I and NIR-II Biowindows, *J. Am. Chem. Soc.*, 2017, **139**(45), 16235–16247, DOI: **10.1021/jacs.7b07818**.

12 J. Xuan, Z. Wang, Y. Chen, D. Liang, L. Cheng, X. Yang, Z. Liu, R. Ma, T. Sasaki and F. Geng, Organic-base-driven Intercalation and Delamination for the Production of Functionalized

Titanium Carbide Nanosheets with Superior Photothermal Therapeutic Performance, *Angew. Chem., Int. Ed.*, 2016, **128**(47), 14789–14794.

13 Y. Ren, G. Li, H. An, S. Wei, C. Xing and Z. Peng, Interface Engineering SnS2/MXene Nb2C Self-Powered Photodetectors with High Responsivity and Detectivity, *Appl. Surf. Sci.*, 2023, **637**, 157863, DOI: **10.1016/j.apsusc.2023.157863**.

14 Y. Gogotsi and B. Anasori, The Rise of MXenes, *ACS Nano*, 2019, **13**(8), 8491–8494.

15 M. Askkar Deen, H. Kumar Rajendran, R. Chandrasekar, D. Ghosh and S. Narayanasamy, The Rise of $Ti_3C_2T_x$ MXene Synthesis Strategies over the Decades: A Review, *FlatChem*, 2024, **47**, 100734, DOI: **10.1016/j.flatc.2024.100734**.

16 J. Zhou, N. Zhang, J. Liu, Q. Gao, Y. Zhang, F. Gao, P. Hu and W. Feng, The Rise of 2D Materials-Based Photoelectrochemical Photodetectors: Progress and Prospect, *Adv. Opt. Mater.*, 2024, **12**(22), 2400706, DOI: **10.1002/adom.202400706**.

17 D. Wang, X. Liu, Y. Kang, X. Wang, Y. Wu, S. Fang, H. Yu, M. H. Memon, H. Zhang, W. Hu, Z. Mi, L. Fu, H. Sun and S. Long, Bidirectional Photocurrent in p–n Heterojunction Nanowires, *Nat. Electron.*, 2021, **4**(9), 645–652, DOI: **10.1038/s41928-021-00640-7**.

18 Y. Zhang, Y. Xu, L. Gao, X. Liu, Y. Fu, C. Ma, Y. Ge, R. Cao, X. Zhang, O. A. Al-Hartomy, S. Wageh, A. Al-Ghamdi, H. Algarni, Z. Shi and H. Zhang, MXene-Based Mixed-Dimensional Schottky Heterojunction towards Self-Powered Flexible High-Performance Photodetector, *Mater. Today Phys.*, 2021, **21**, 100479, DOI: **10.1016/j.mtphys.2021.100479**.

19 L. Gao, C. Ma, S. Wei, A. V. Kuklin, H. Zhang and H. Ågren, Applications of Few-Layer Nb_2C MXene: Narrow-Band Photodetectors and Femtosecond Mode-Locked Fiber Lasers, *ACS Nano*, 2021, **15**(1), 954–965, DOI: **10.1021/acsnano.0c07608**.

20 Z. Liu, J. K. El-Demellawi, O. M. Bakr, B. S. Ooi and H. N. Alshareef, Plasmonic Nb_2CT_x MXene-$MAPbI_3$ Heterostructure for Self-Powered Visible-NIR Photodiodes, *ACS Nano*, 2022, **16**(5), 7904–7914, DOI: **10.1021/acsnano.2c00558**.

21 S. Zhou, C. Jiang, J. Han, Y. Mu, J. R. Gong, J. Zhang and P. E. C. High-Performance Self-Powered, Photodetectors Based on 2D $BiVO_4$/MXene Schottky Junction, *Adv. Funct. Mater.*, 2024, 2416922, DOI: **10.1002/adfm.202416922**.

22 J. Azadmanjiri, P. K. Roy, L. Děkanovský, J. Regner and Z. Sofer, $Ti_3C_2T_x$ MXene Anchoring Semi-Metallic Selenium Atoms: Self-Powered Photoelectrochemical-Type Photodetector, Hydrogen Evolution, and Gas-Sensing Applications, *2D Mater.*, 2022, **9**(4), 045019, DOI: **10.1088/2053-1583/ac88e2**.

23 S. Huang and V. N. Mochalin, Understanding Chemistry of Two-Dimensional Transition Metal Carbides and Carbonitrides (MXenes) with Gas Analysis, *ACS Nano*, 2020, **14**(8), 10251–10257, DOI: **10.1021/acsnano.0c03602**.

24 Z. Ling, C. E. Ren, M.-Q. Zhao, J. Yang, J. M. Giammarco, J. Qiu, M. W. Barsoum and Y. Gogotsi, Flexible and Conductive MXene Films and Nanocomposites with High Capacitance, *Proc. Natl. Acad. Sci. U. S. A.*, 2014, **111**(47), 16676–16681, DOI: **10.1073/pnas.1414215111**.

25 I. J. Echols, J. Yun, H. Cao, R. M. Thakur, A. Sarmah, Z. Tan, R. Littleton, M. Radovic, M. J. Green and J. L. Lutkenhaus, Conformal Layer-by-Layer Assembly of $Ti_3C_2T_z$ MXene-Only Thin Films for Optoelectronics and Energy Storage, *Chem. Mater.*, 2022, **34**(11), 4884–4895, DOI: **10.1021/acs.chemmater.1c04394**.

26 M. A. K. Purbayanto, D. Bury, M. Chandel, Z. D. Shahrak, V. N. Mochalin, A. Wójcik, D. Moszczyńska, A. Wojciechowska, A. Tabassum, M. Naguib and A. M. Jastrzębska, Ambient Processed rGO/Ti_3CNT_x MXene Thin Film with High Oxidation Stability, Photosensitivity, and Self-Cleaning Potential, *ACS Appl. Mater. Interfaces*, 2023, **15**(37), 44075–44086, DOI: **10.1021/acsami.3c07972**.

27 B. Hwang, M. Park, T. Kim and S. Han, Effect of RGO Deposition on Chemical and Mechanical Reliability of Ag Nanowire Flexible Transparent Electrode, *RSC Adv.*, 2016, **6**(71), 67389–67395, DOI: **10.1039/C6RA10338C**.

28 C. Xu, F. Yang, B. Deng, S. Che, W. Yang, G. Zhang, Y. Sun and Y. Li, RGO-Wrapped Ti_3C_2/TiO_2 Nanowires as a Highly Efficient Photocatalyst for Simultaneous Reduction of Cr(VI) and Degradation of RhB under Visible Light Irradiation, *J. Alloys Compd.*, 2021, **874**, 159865, DOI: **10.1016/j.jallcom.2021.159865**.

29 A. M. Dimiev, L. B. Alemany and J. M. Tour, Graphene Oxide. Origin of Acidity, Its Instability in Water, and a New Dynamic Structural Model, *ACS Nano*, 2013, **7**(1), 576–588, DOI: **10.1021/nn3047378**.

30 Y. Wang, Y. Wang, K. Chen, K. Qi, T. Xue, H. Zhang, J. He and S. Xiao, Niobium Carbide MXenes with Broad-Band Nonlinear Optical Response and Ultrafast Carrier Dynamics, *ACS Nano*, 2020, **14**(8), 10492–10502, DOI: **10.1021/acsnano.0c04390**.

31 B. Shen, X. Liao, X. Zhang, H.-T. Ren, J.-H. Lin, C.-W. Lou and T.-T. Li, Synthesis of Nb_2C MXene-Based 2D Layered Structure Electrode Material for High-Performance Battery-Type Supercapacitors, *Electrochim. Acta*, 2022, **413**, 140144, DOI: **10.1016/j.electacta.2022.140144**.

32 S. Thakur, A. Badoni, Samriti, P. Sharma, A. Ojha, H. C. Swart, A. Y. Kuznetsov and J. Prakash, Standalone Highly Efficient Graphene Oxide as an Emerging Visible Light-Driven Photocatalyst and Recyclable Adsorbent for the Sustainable Removal of Organic Pollutants, *Langmuir*, 2024, **40**(35), 18486–18502, DOI: **10.1021/acs.langmuir.4c01727**.

33 S. Obata, H. Tanaka and K. Saiki, Electrical and Spectroscopic Investigations on the Reduction Mechanism of Graphene Oxide, *Carbon*, 2013, **55**, 126–132, DOI: **10.1016/j.carbon.2012.12.018**.

34 A. Morais, J. P. C. Alves, F. A. S. Lima, M. Lira-Cantu and A. F. Nogueira, Enhanced Photovoltaic Performance of Inverted Hybrid Bulk-Heterojunction Solar Cells Using TiO_2/Reduced Graphene Oxide Films as Electron Transport Layers, *J. Photonics Energy*, 2015, **5**(1), 057408, DOI: **10.1117/1.JPE.5.057408**.

35 W. Zhou, B. Yu, J. Zhu, K. Li and S. Tian, Hierarchical ZnO/MXene (Nb_2C and V_2C) Heterostructure with Efficient

Electron Transfer for Enhanced Photocatalytic Activity, *Appl. Surf. Sci.*, 2022, **590**, 153095, DOI: 10.1016/j.apsusc.2022.153095.

36 J. Halim, K. M. Cook, M. Naguib, P. Eklund, Y. Gogotsi, J. Rosen and M. W. Barsoum, X-Ray Photoelectron Spectroscopy of Select Multi-Layered Transition Metal Carbides (MXenes), *Appl. Surf. Sci.*, 2016, **362**, 406–417.

37 S. Byun, B. Kim, S. Jeon and B. Shin, Effects of a SnO_2 Hole Blocking Layer in a BiVO4-Based Photoanode on Photoelectrocatalytic Water Oxidation, *J. Mater. Chem. A*, 2017, **5**(15), 6905–6913, DOI: 10.1039/C7TA00806F.

38 A. N. Giordano, J. Jiang, A. Advincula, K. Shevchuk, M. S. Carey, T. C. Back, Y. Gogotsi, D. Nepal, R. Pachter and R. Rao, Raman Spectroscopy and Laser-Induced Surface Modification of Nb_2CT_x MXene, *ACS Mater. Lett.*, 2024, **6**(8), 3264–3271, DOI: 10.1021/acsmaterialslett.4c00922.

39 T. Hu, M. Hu, B. Gao, W. Li and X. Wang, Screening Surface Structure of MXenes by High-Throughput Computation and Vibrational Spectroscopic Confirmation, *J. Phys. Chem. C*, 2018, **122**(32), 18501–18509, DOI: 10.1021/acs.jpcc.8b04427.

40 A. C. Ferrari and J. Robertson, Interpretation of Raman Spectra of Disordered and Amorphous Carbon, *Phys. Rev. B*, 2000, **61**(20), 14095–14107, DOI: 10.1103/PhysRevB.61.14095.

41 T. Su, R. Peng, Z. D. Hood, M. Naguib, I. N. Ivanov, J. K. Keum, Z. Qin, Z. Guo and Z. Wu, One-step Synthesis of Nb_2O_5/C/Nb_2C (MXene) Composites and Their Use as Photocatalysts for Hydrogen Evolution, *ChemSusChem*, 2018, **11**(4), 688–699, DOI: 10.1002/cssc.201702317.

42 H. Cheng and W. Zhao, Regulating the Nb_2C Nanosheets with Different Degrees of Oxidation in Water Lubricated Sliding toward an Excellent Tribological Performance, *Friction*, 2022, **10**(3), 398–410, DOI: 10.1007/s40544-020-0469-x.

43 A. Wróblewska, A. Dużyńska, J. Judek, L. Stobiński, K. Żerańska, A. P. Gertych and M. Zdrojek, Statistical Analysis of the Reduction Process of Graphene Oxide Probed by Raman Spectroscopy Mapping, *J. Phys.: Condens. Matter*, 2017, **29**(47), 475201, DOI: 10.1088/1361-648X/aa92fe.

44 Y. Cao, Z. Wang, Q. Bian, Z. Cheng, Z. Shao, Z. Zhang, H. Sun, X. Zhang, S. Li, H. Gedeon, L. Liu, X. Wang, H. Yuan and M. Pan, Phonon Modes and Photonic Excitation Transitions of MoS_2 Induced by Top-Deposited Graphene Revealed by Raman Spectroscopy and Photoluminescence, *Appl. Phys. Lett.*, 2019, **114**(13), 133103, DOI: 10.1063/1.5083104.

45 N. Ma, C. Lu, Y. Liu, T. Han, W. Dong, D. Wu and X. Xu, Direct Z-Scheme Heterostructure of Vertically Oriented SnS_2 Nanosheet on $BiVO_4$ Nanoflower for Self-Powered Photodetectors and Water Splitting, *Small*, 2024, **20**(3), 2304839, DOI: 10.1002/smll.202304839.

46 M. K. Rabchinskii, V. V. Shnitov, A. T. Dideikin, A. E. Aleksenskii, S. P. Vul', M. V. Baidakova, I. I. Pronin, D. A. Kirilenko, P. N. Brunkov, J. Weise and S. L. Molodtsov, Nanoscale Perforation of Graphene Oxide during Photoreduction Process in the Argon Atmosphere, *J. Phys. Chem. C*, 2016, **120**(49), 28261–28269, DOI: 10.1021/acs.jpcc.6b08758.

47 M. K. Rabchinskii, A. T. Dideikin, D. A. Kirilenko, M. V. Baidakova, V. V. Shnitov, F. Roth, S. V. Konyakhin, N. A. Besedina, S. I. Pavlov, R. A. Kuricyn, N. M. Lebedeva, P. N. Brunkov and A. Y. Vul', Facile Reduction of Graphene Oxide Suspensions and Films Using Glass Wafers, *Sci. Rep.*, 2018, **8**(1), 14154, DOI: 10.1038/s41598-018-32488-x.

48 A. Kudo, H. Yanagi, K. Ueda, H. Hosono, H. Kawazoe and Y. Yano, Fabrication of Transparent p–n Heterojunction Thin Film Diodes Based Entirely on Oxide Semiconductors, *Appl. Phys. Lett.*, 1999, **75**(18), 2851–2853, DOI: 10.1063/1.125171.

49 H. An, T. Habib, S. Shah, H. Gao, M. Radovic, M. J. Green and J. L. Lutkenhaus, Surface-Agnostic Highly Stretchable and Bendable Conductive MXene Multilayers, *Sci. Adv.*, 2018, **4**(3), eaaq0118, DOI: 10.1126/sciadv.aaq0118.

50 G. Chang, L. Zeng, L. Xie, B. Xue and Q. Zheng, Ultrathin Multifunctional Electromagnetic Interference Shielding MXene/AgNWs/PEDOT:PSS Coatings with Superior Electro/Photo-Thermal Transition Ability and Water Repellency, *Chem. Eng. J.*, 2023, **470**, 144033, DOI: 10.1016/j.cej.2023.144033.

51 K. Karmakar, P. Sarkar, J. Sultana, N. Kurra and K. D. M. Rao, Layer-by-Layer Assembly-Based Heterointerfaces for Modulating the Electronic Properties of $Ti_3C_2T_x$ MXene, *ACS Appl. Mater. Interfaces*, 2021, **13**(49), 59104–59114, DOI: 10.1021/acsami.1c18471.

52 T. Habib, X. Zhao, S. A. Shah, Y. Chen, W. Sun, H. An, J. L. Lutkenhaus, M. Radovic and M. J. Green, Oxidation Stability of $Ti_3C_2T_x$ MXene Nanosheets in Solvents and Composite Films, *NPJ 2D Mater. Appl.*, 2019, **3**(1), 1–6, DOI: 10.1038/s41699-019-0089-3.

53 T. B. Limbu, B. Chitara, J. D. Orlando, M. Y. Garcia Cervantes, S. Kumari, Q. Li, Y. Tang and F. Yan, Green Synthesis of Reduced $Ti_3C_2T_x$ MXene Nanosheets with Enhanced Conductivity, Oxidation Stability, and SERS Activity, *J. Mater. Chem. C*, 2020, **8**(14), 4722–4731, DOI: 10.1039/C9TC06984D.

54 K. Liang, T. Wu, S. Misra, C. Dun, S. Husmann, K. Prenger, J. J. Urban, V. Presser, R. R. Unocic, D. Jiang and M. Naguib, Nitrogen-Doped Graphene-Like Carbon Intercalated MXene Heterostructure Electrodes for Enhanced Sodium- and Lithium-Ion Storage, *Adv. Sci.*, 2024, **11**(31), 2402708, DOI: 10.1002/advs.202402708.

55 S. Adomaviciute-Grabusove, A. Popov, S. Ramanavicius, V. Sablinskas, K. Shevchuk, O. Gogotsi, I. Baginskiy, Y. Gogotsi and A. Ramanavicius, Monitoring $Ti_3C_2T_x$ MXene Degradation Pathways Using Raman Spectroscopy, *ACS Nano*, 2024, **18**(20), 13184–13195, DOI: 10.1021/acsnano.4c02150.

56 T. Guo, D. Zhou, S. Deng, M. Jafarpour, J. Avaro, A. Neels, J. Heier and C. Zhang, Rational Design of $Ti_3C_2T_x$ MXene Inks for Conductive, Transparent Films, *ACS Nano*, 2023, **17**(4), 3737–3749, DOI: 10.1021/acsnano.2c11180.

57 Y. Gao, Y. S. Zhou, W. Xiong, L. J. Jiang, M. Mahjourisamani, P. Thirugnanam, X. Huang, M. M. Wang, L. Jiang and Y. F. Lu, Transparent, Flexible, and Solid-State

Supercapacitors Based on Graphene Electrodes, *APL Mater.*, 2013, **1**(1), 012101, DOI: 10.1063/1.4808242.

58 J.-S. M. Lee, M. E. Briggs, C.-C. Hu and A. I. Cooper, Controlling Electric Double-Layer Capacitance and Pseudocapacitance in Heteroatom-Doped Carbons Derived from Hypercrosslinked Microporous Polymers, *Nano Energy*, 2018, **46**, 277–289, DOI: 10.1016/j.nanoen.2018.01.042.

59 B. Koo, S. Byun, S.-W. Nam, S.-Y. Moon, S. Kim, J. Y. Park, B. T. Ahn and B. Shin, Reduced Graphene Oxide as a Catalyst Binder: Greatly Enhanced Photoelectrochemical Stability of Cu(In,Ga)Se2 Photocathode for Solar Water Splitting, *Adv. Funct. Mater.*, 2018, **28**(16), 1705136, DOI: 10.1002/adfm.201705136.

60 L. Liu, L. Huang, S. Yan, W. Shi, S. Li, X. Chen and J. Liu, Heteroatom Doped S, N-MXene/rGO Flexible Film for Supercapacitor Applications, *Chem. Eng. J.*, 2025, **506**, 160320, DOI: 10.1016/j.cej.2025.160320.

61 J. Zhang, Z. Xiong, Z. Wang and J. Sun, Study on the Preparation and PEC-Type Photodetection Performance of β-Bi_2O_3 Thin Films, *Materials*, 2024, **17**(15), 3779, DOI: 10.3390/ma17153779.

62 J. Bisquert, C. Gonzales and A. Guerrero, Transient On/Off Photocurrent Response of Halide Perovskite Photodetectors, *J. Phys. Chem. C*, 2023, **127**(43), 21338–21350, DOI: 10.1021/acs.jpcc.3c04672.

63 N. Zhang, X. Gao, H. Guan, S. Sun, J. Liu, Z. Shao, Q. Gao, Y. Zhang, R. Sun, G. Yang, F. Gao and W. Feng, Three-Dimensional Porous In_2O_3 Arrays for Self-Powered Transparent Solar-Blind Photodetectors with High Responsivity and Excellent Spectral Selectivity, *Nano Res.*, 2024, **17**(5), 4471–4477, DOI: 10.1007/s12274-023-6370-y.

64 M. Jiang, Y. Zhao, L. Bian, W. Yang, J. Zhang, Y. Wu, M. Zhou, S. Lu and H. Qin, Self-Powered Photoelectrochemical (Al,Ga)N Photodetector with an Ultrahigh Ultraviolet/Visible Reject Ratio and a Quasi-Invisible Functionality for 360° Omnidirectional Detection, *ACS Photonics*, 2021, **8**(11), 3282–3290, DOI: 10.1021/acsphotonics.1c01105.

65 J. Zhang, M. Jiang, L. Bian, D. Wu, H. Qin, W. Yang, Y. Zhao, Y. Wu, M. Zhou and S. Lu, A Self-Powered Transparent Photodetector Based on Detached Vertical (In,Ga)N Nanowires with 360° Omnidirectional Detection for Underwater Wireless Optical Communication, *Nanomaterials*, 2021, **11**(11), 2959, DOI: 10.3390/nano11112959.

66 T. H. Park, S. Yu, M. Koo, H. Kim, E. H. Kim, J.-E. Park, B. Ok, B. Kim, S. H. Noh, C. Park, E. Kim, C. M. Koo and C. Park, Shape-Adaptable 2D Titanium Carbide (MXene) Heater, *ACS Nano*, 2019, **13**(6), 6835–6844, DOI: 10.1021/acsnano.9b01602.

67 N. Coca-Lopez, An Intuitive Approach for Spike Removal in Raman Spectra Based on Peaks' Prominence and Width, *Anal. Chim. Acta*, 2024, **1295**, 342312, DOI: 10.1016/j.aca.2024.342312.

68 T. Li, W. Luo, H. Kitadai, X. Wang and X. Ling, Probing the Domain Architecture in 2D α-Mo2C via Polarized Raman Spectroscopy, *Adv. Mater.*, 2019, **31**(8), 1807160, DOI: 10.1002/adma.201807160.

69 J. Yun, I. Echols, P. Flouda, S. Wang, A. Easley, X. Zhao, Z. Tan, E. Prehn, G. Zi, M. Radovic, M. J. Green and J. L. Lutkenhaus, Layer-by-Layer Assembly of Polyaniline Nanofibers and MXene Thin-Film Electrodes for Electrochemical Energy Storage, *ACS Appl. Mater. Interfaces*, 2019, **11**(51), 47929–47938, DOI: 10.1021/acsami.9b16692.

